NEUROSCIENCE

Elastocapillary self-assembled neurotassels for stable neural activity recordings

S. Guan[1,2,3]*, J. Wang[1,2]*, X. Gu[2,3]*, Y. Zhao[4], R. Hou[2], H. Fan[2], L. Zou[1,3], L. Gao[1,3], M. Du[1,3], C. Li[2]†, Y. Fang[1,2]†

Implantable neural probes that are mechanically compliant with brain tissue offer important opportunities for stable neural interfaces in both basic neuroscience and clinical applications. Here, we developed a Neurotassel consisting of an array of flexible and high–aspect ratio microelectrode filaments. A Neurotassel can spontaneously assemble into a thin and implantable fiber through elastocapillary interactions when withdrawn from a molten, tissue-dissolvable polymer. Chronically implanted Neurotassels elicited minimal neuronal cell loss in the brain and enabled stable activity recordings of the same population of neurons in mice learning to perform a task. Moreover, Neurotassels can be readily scaled up to 1024 microelectrode filaments, each with a neurite-scale cross-sectional footprint of 3 × 1.5 μm^2, to form implantable fibers with a total diameter of ~100 μm. With their ultrasmall sizes, high flexibility, and scalability, Neurotassels offer a new approach for stable neural activity recording and neuroprosthetics.

INTRODUCTION

Implantable neural probes are the most widely used tool for recording neural activity at single-cell, submillisecond resolution (*1*–*9*), but their signals tend to degrade over time because of chronic tissue response and neuronal cell loss around the implant site (*10*–*15*). The failure of implanted neural probes for chronic recordings poses one of the most critical challenges in both longitudinal studies of cognitive functions, such as learning and memory, and high-fidelity neural prosthetics. Experimental evidence suggests that flexible neural probes that are compliant with brain tissues can reduce relative shear motion, leading to improved stability of neural interfaces (*16*–*27*). However, flexible neural probes are susceptible to bending, buckling, and deflecting during insertion into the brain. A variety of strategies have been developed to briefly increase their stiffness for tissue insertion, including removable insertion shuttles (*20*, *27*, *28*), polymer molds (*29*–*31*), and integrated microfluidic devices (*32*, *33*). Because of constraints on implantation footprints and tissue lesions, the number of recording channels per flexible probe in these studies has been generally limited to below 100 (*25*, *27*, *31*, *34*), whereas silicon Neuropixels can provide 960 addressable sites per shank (*9*). Recent work demonstrated that 128-channel flexible macroporous mesh microelectrode probes can be injected through 650-μm-diameter glass needles (*35*). Nevertheless, further increasing the channel number of flexible neural probes while minimizing their implantation footprints remains challenging.

Elastocapillary self-assembly (*36*, *37*) is an efficient and scalable process to arrange flexible and high–aspect ratio building blocks into ordered structures by long-range capillary forces and has been widely observed both in natural systems, such as wet hair, and in engineered systems that range from micropillars to carbon nanotubes (*38*–*40*). In this study, we developed a Neurotassel probe that combines the simplicity and efficiency of elastocapillary self-assembly with the precision and scalability of microfabrication. Chronically implanted Neurotassels were able to record the same neuronal population in mice throughout learning of a working memory task. The stable monitoring of the same neurons across time allowed us to identify diverse patterns of learning-related activity modulation in the medial prefrontal cortex (mPFC). Furthermore, Neurotassels were easily assembled with optical fibers for simultaneous optogenetic stimulation and electrical recordings.

[1]CAS Key Laboratory for Biomedical Effects of Nanomaterials and Nanosafety, CAS Center for Excellence in Nanoscience, National Center for Nanoscience and Technology, Beijing 100190, China. [2]CAS Center for Excellence in Brain Science and Intelligence Technology, Institute of Neuroscience, Shanghai Institutes for Biological Sciences, Chinese Academy of Sciences, Shanghai 200031, China. [3]University of Chinese Academy of Sciences, Beijing 100049, China. [4]College of Mechanical and Vehicle Engineering, Hunan University, Changsha 410082, China.
*These authors contributed equally to this work.
†Corresponding author. Email: tonylicy@ion.ac.cn (C.L.); fangy@nanoctr.cn (Y.F.)

RESULTS

Fabrication and elastocapillary self-assembly of Neurotassels

The Neurotassels were fabricated on silicon substrates by using standard microfabrication processes (fig. S1). As shown in Fig. 1A, fig. S2, and movie S1, a typical Neurotassel consists of a freestanding segment, with a total thickness of 1.5 to 3 μm, connected electrically to substrate-supported bonding pads. Longitudinal microelectrodes (100-nm-thick Au) are encapsulated between two polyimide (PI) layers, except the recording sites at the front end (Fig. 1B). The electrical connection between Neurotassels and measurement electronics was realized using flip chip–bonded flexible printed circuits (FPCs) (fig. S3). The freestanding segment of the Neurotassel has a plane-mesh-filament structure design, so that the effective transverse bending stiffness per unit length decreases successively from 6 to 0.8 to <0.1 nN·m. As shown by finite element (FE) simulation results in Fig. 1C and fig. S4, the plane-mesh-filament design not only improves the structural integrity of the Neurotassel but also prearranges the filaments into a radial array during elastic deformation.

To induce elastocapillary self-assembly, we progressively withdrawn a Neurotassel from a bath of molten polyethylene glycol (PEG) 4000 at 120°C into ambient air, as shown schematically in Fig. 1D. During the drawing process, the molten PEG film that adhered to the Neurotassel retracted to assume a circular shape under surface tension γ, and the capillary force accordingly deformed the elastic Neurotassel as characterized by its bending stiffness *B* (fig. S5). The PEG quickly solidified in ambient air, resulting in the formation of a stiff Neurotassel/PEG assembly. Figure 1E and movie S2 show the successive deformation of a Neurotassel driven mainly by the interplay between elastic and capillary forces. The mesh section of the Neurotassel formed a series of puffs, whereas the high–aspect ratio filaments were pulled together to

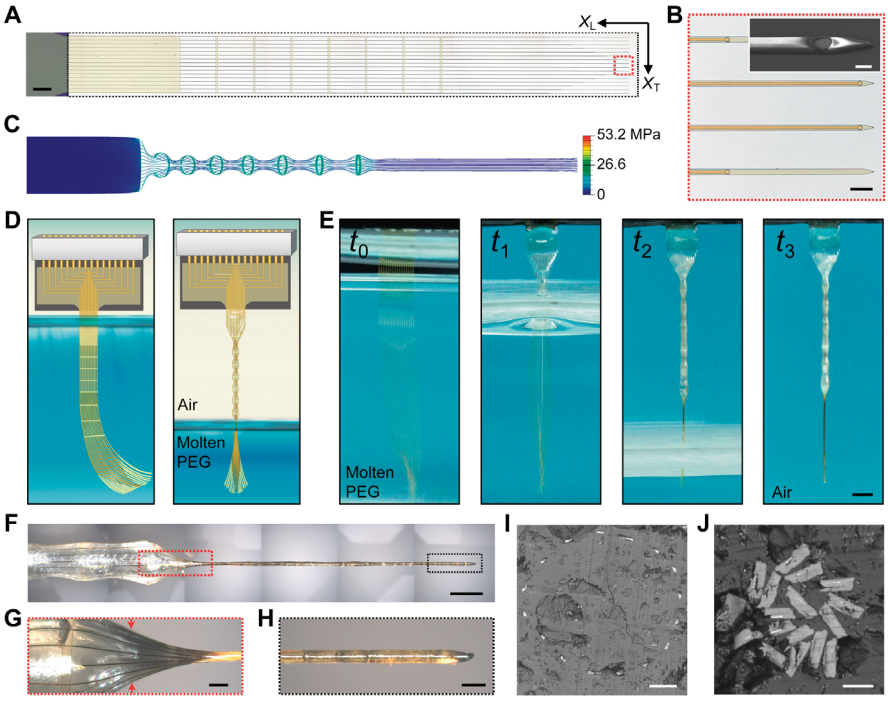

Fig. 1. Elastocapillary self-assembly of Neurotassels. (**A**) An as-fabricated 16-channel Neurotassel. The black dashed box highlights the freestanding segment supported on an aluminum release layer. X_T and X_L are the transverse and longitudinal directions, respectively. Scale bar, 500 μm. (**B**) Zoom-in view of 12-μm-wide and 3-μm-high microelectrode filaments, as marked by the dashed red box in (A). Scale bar, 50 μm. Inset: Scanning electron microscopy (SEM) image of a microelectrode filament with a 10-μm-diameter recording site. Scale bar, 10 μm (inset). (**C**) Simulated von Mises stresses in a deformed Neurotassel. (**D**) Schematics of the elastocapillary self-assembly of a Neurotassel. (**E**) Time sequence photographs of the elastocapillary self-assembly of a Neurotassel. Scale bar, 1 mm. (Photo credit: Shouliang Guan and Jinfen Wang at NCNST). (**F**) A Neurotassel/PEG assembly. Scale bar, 500 μm. (**G** and **H**) Zoom-in views of the Neurotassel/PEG assembly as marked by the red and black dashed boxes, respectively, in (F). Scale bars, 100 μm. (**I**) Cross-sectional image at the mesh-filament transition section, indicated by the red arrows in (G). Scale bar, 50 μm. (**J**) Cross-sectional image of the fiber. Scale bar, 10 μm.

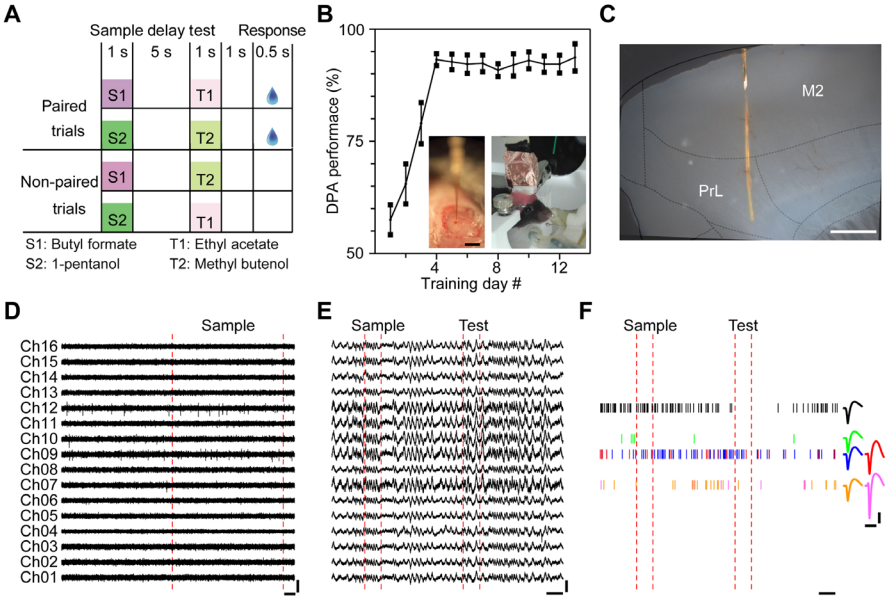

Fig. 2. Recordings by Neurotassels during DPA tasks. (**A**) Schematic of the olfactory DPA task. (**B**) Performance of mice trained with the DPA task. Insets: An implanted 16-channel Neurotassel (left) and a mouse with an implanted Neurotassel in the mPFC (right). Error bars represent SD around the mean (n = 6). Scale bar, 1 mm (inset). (Photo credit: Xiaowei Gu at ION). (**C**) Microphoto of a 200-μm-thick brain slice with an implanted Neurotassel. The mouse brain was sliced in sagittal direction and parallel to the implanted Neurotassel. Anatomical borders were identified according to the stereotaxic atlas of Paxinos and Watson (2001). Scale bar, 500 μm. (**D**) Extracellular AP traces (250 to 8000 Hz) recorded by a 16-channel Neurotassel implanted in the mPFC of M04. Scale bars, 200 μV (vertical), 100 ms (horizontal). (**E**) LFP traces (0.5 to 200 Hz) during a task trial. Scale bars, 300 μV (vertical), 1 s (horizontal). (**F**) Spike rasters of isolated neurons during a task trial. Scale bars, 50 μV (vertical), 1 s and 1 ms (horizontal; left and right, respectively).

form a straight and thin fiber with a total diameter of 55 μm (Fig. 1, F to H). Figure 1I shows the cross-sectional image at the mesh-filament transition zone, in which the filaments are radially arranged in a circular shape. Figure 1J illustrates the cross-sectional image of the thin fiber, showing 16 microelectrode filaments embedded in PEG.

Stable neural activity tracking by Neurotassels during delayed pair association tasks

We first examined the depth implantation of Neurotassels in mice. Assembled Neurotassel/PEG fibers can be feasibly implanted into the targeted brain regions of mice because of the stiffening effect of the PEG (movie S3). Platinum electrodeposition was applied to Neurotassels before implantation to increase the effective surface area of the microelectrodes and reduce their impedance from >1 megohm to ~50 kilohm at 1 kHz (fig. S2C). Following implantation, PEG was dissolved by body fluids in the brain tissue (*41*), and the Neurotassels were released and transformed back to highly flexible microelectrode filaments (fig. S6 and movie S4). The electrical integrity of the Neurotassels was maintained after implantation, with a device yield exceeding 95%.

Stable recording of the same population of neurons throughout behavioral training is of great importance for both understanding the dynamic functions of neurons and practical applications of the brain-machine interface. We therefore tested the ability of the Neurotassels to stably record neuronal activities from mice during behavioral training. The mice were trained to perform a working memory task. The task required the mice to retain information during a delay period (*42*). Our previous study revealed prominent delay period activity modulation of the mPFC neurons during the learning, but not the well-trained, phase (*43*). These former results were obtained by advancing microwire tetrodes a small distance each day, with the activity profiles of different

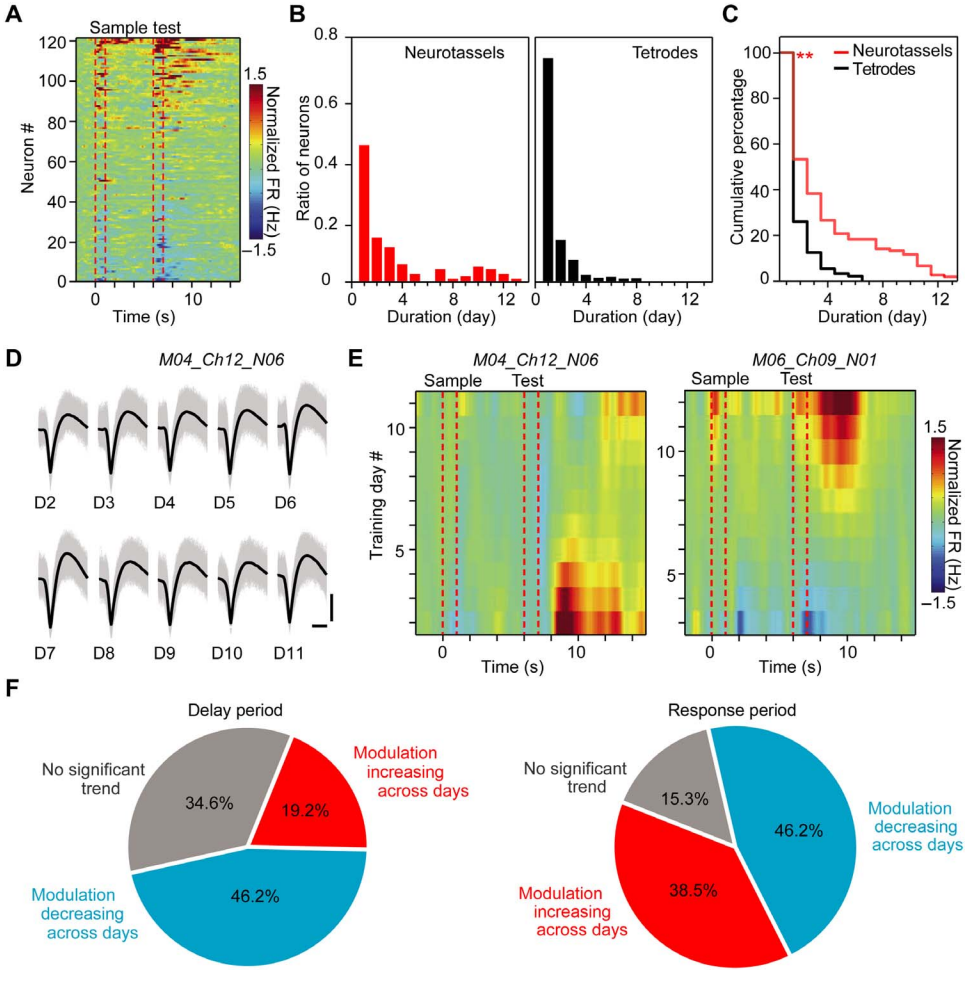

Fig. 3. Recording stability during DPA tasks. (**A**) Heat map of normalized firing rates (FRs) for the recorded neurons by Neurotassels during training. Each row represents the baseline-normalized firing rate of one neuron. The dashed red lines represent the onsets and offsets of odor delivery. (**B**) Distribution of neurons according to the continuously recorded duration days by Neurotassels (left) and microwire tetrodes (right), respectively. One hundred twenty-one (121) neurons were recorded by six Neurotassels from six mice, and 730 neurons were recorded by 256 tetrodes from eight mice. Each tetrode was constructed by twisting four PI-insulated, Ni-Chrome wires with a 12.5-μm-diameter core. (**C**) Cumulative distribution of the percentage of neurons as a function of recording duration showing significant increases in recording of Neurotassels (red line) compared with that of tetrodes (black line) (**$P < 0.01$, Kolmogorov-Smirnov test). (**D**) The waveforms of an example neuron stably recorded during the training process. Scale bars, 50 μV (vertical), 0.5 ms (horizontal). (**E**) Heat map of the normalized firing rate for two example neurons. Each row represents the baseline-normalized firing rate of one training day. (**F**) Percentage of neurons with an increase or a decrease in firing through training during the delay (left) and response (right) periods, respectively. Twenty-six (26) neurons that were continuously recorded for longer than 5 days were considered here.

neurons compared at different phases. To follow the activity modulation of the same neurons throughout training, we implanted Neurotassels into the mPFC of mice ($n = 6$) and then trained the mice to perform an olfactory delayed pair association (DPA) task (*44*) for 13 days (Fig. 2A and fig. S7A). Specifically, head-fixed mice were required to retain the memory of a sample odor (S1 or S2) for a delay period of 5 s, after which a test odor (T1 or T2) was delivered. Water-restricted mice were rewarded with water if they licked within a response window in the paired trials (S1-T1 or S2-T2). The performance correct rate of the mice steadily increased during the first 4 days of training (learning phase) and then stabilized at ~90% correct for the following 9 days (well-trained phase) (Fig. 2B).

The mPFC neuronal activities were recorded by Neurotassels each day throughout training (Fig. 2C). Figure 2 (D and E) shows representative multichannel recordings of action potential (AP) and local field potential (LFP), respectively, during a task trial by a 16-channel Neurotassel implanted in a mouse (M04) on training day 5. From the AP recording, six neurons were isolated (Fig. 2F). Overall, we recorded 121 neurons with the Neurotassels during training (fig. S8) and observed a strong modulation in the population activity profile by the DPA task (Fig. 3A). Notably, 21 and 12% of the 121 neurons could be repeatedly recorded by the Neurotassels for over 5 and 10 days, respectively (Fig. 3, B to D). This is in contrast to the results obtained with the microwire tetrodes, from which only 4% neurons were repeatedly recorded for more than 5 days. The stable monitoring of the same neurons across time revealed that the mPFC neurons exhibited diverse patterns of learning-related activity modulation (either decrease or increase) (Fig. 3E and fig. S9). Overall, more neurons exhibited a reduced activity modulation during the sample delivery and delay periods after the mice were well trained (Fig. 3F), consistent with our previous finding that delay period activity of the mPFC is only important during learning of an olfactory delayed nonmatched to sample (DNMS) task (*43*). During the response period, however, there were similar numbers of neurons with an increased or a decreased modulation in activity. This result indicates that the neuronal activity of the mPFC during the decision-making period of the DNMS task is still actively modulated in the well-trained phase. Thus, the Neurotassels were able to reveal the dynamic activity profiles of the same neurons during learning of a working memory task.

LFPs carry important information within a local network or across brain regions (*45*). We implanted two assembled Neurotassel/PEG fibers into the anterior and posterior piriform cortex (denoted as aPC and pPC, respectively) to measure the temporal relationship between sensory-driven LFPs of the two regions (fig. S7, B and C). The aPC and pPC regions were selected for their importance in coding of olfactory information (*46*). During the odor delivery period, we observed an increased power in the β (13 to 30 Hz) and γ (30 to 80 Hz) bands at both regions (fig. S7, D and E). Moreover, the coherence in the γ range between the two regions was increased during odor delivery (fig. S7F).

Integration of Neurotassels with optical fibers for dual-functional probes

The flexible Neurotassels can be easily assembled on the surface of optical fibers through elastocapillary interactions to form dual-functional probes for simultaneous optogenetic stimulation (*47*) and

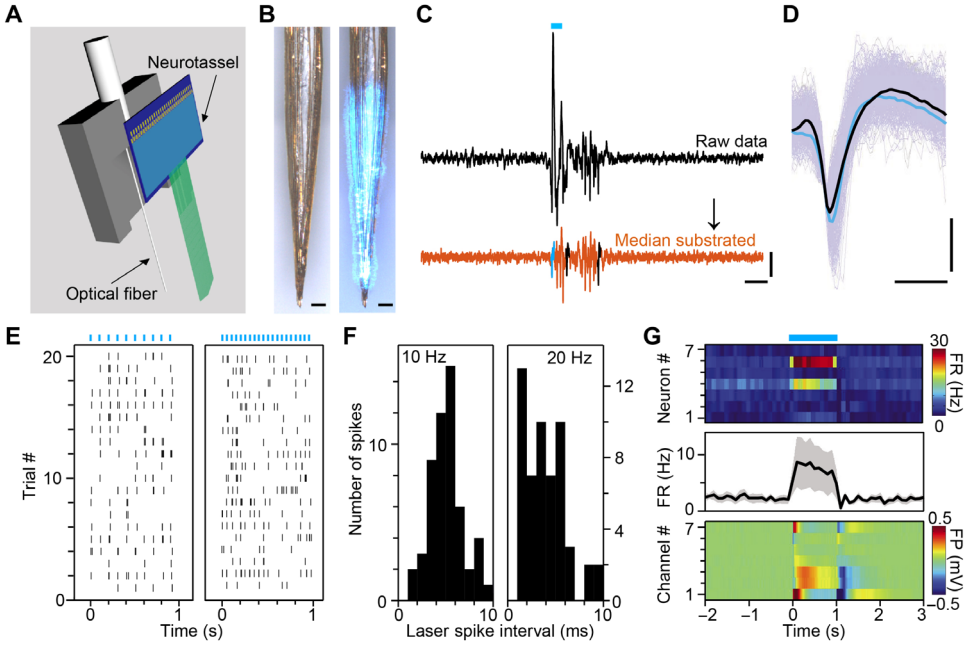

Fig. 4. Simultaneous optogenetic stimulation and electrical recordings. (**A**) Schematic of elastocapillary self-assembly of a Neurotassel on a sharpened optical fiber. (**B**) A 61-channel Neurotassel assembled on a sharpened optical fiber without (left) and with (right) light, respectively. Scale bars, 100 μm. (**C**) Black: Potential trace for a single trial with optogenetic transients at onset and offset of laser stimulation. Orange: Potential trace after subtraction of the median. Scale bars, 0.1 mV (vertical), 10 ms (horizontal). (**D**) Average waveforms of light-evoked (blue) and spontaneous (black) spikes. Scale bars, 50 μV (vertical), 0.5 ms (horizontal). (**E**) Raster plots of evoked spike firing of an example neuron by 10-Hz (left) and 20-Hz (right) 5-ms laser stimulation (marked by blue bars). (**F**) Distribution of spike jitter from laser as measured by the delay from stimulation onset to the first evoked spikes during the 10-Hz (left, total 200 pulses) and 20-Hz (right, total 400 pulses) stimulation. (**G**) Top: Heat map of firing rates of seven neurons in response to 1-s laser stimulation. Middle: Averaged firing rate of the neurons. Bottom: Heat map of field potentials at the recording sites of the neurons.

electrical recording (Fig. 4, A and B). We implanted assembled 61-channel Neurotassel/optical fiber dual-functional probes into the mPFC of transgenic Thy1-ChR2 mice (fig. S10 and movie S5). Figure 4C shows representative electrical signals recorded by a microelectrode during 5-ms-pulse optogenetic stimulation with a 473-nm blue laser. Light-evoked and spontaneous spikes exhibited similar waveforms (Fig. 4D), indicating that they were from the same neuron. As shown in Fig. 4E, the neuron fired reliably in response to 10- and 20-Hz 5-ms stimulation. The short latency of the evoked spikes (for 10 Hz: 3.8 ± 1.9 ms, 110 spikes; for 20 Hz: 2.5 ± 2.1 ms, 178 spikes) indicates that the neuron was directly activated by light (Fig. 4F). Figure 4G summarizes the response of seven recorded neurons to 1-s laser stimulation, two of which were strongly activated by stimulation. These results show that neural activities, including spikes and LFPs, can be reliably recorded by Neurotassels and easily integrated with optogenetics.

Long-term chronic stability of Neurotassels

Next, we evaluated the long-term stability of Neurotassels. Neuronal activity recordings were performed by 16-channel Neurotassels implanted in the mPFC of mice (n = 7) from 3 to 6 weeks after implantation (Fig. 5, A to C, fig. S11, and movie S6). The Neurotassels isolated 36 and 28 sortable neurons from seven mice at 3 and 4 weeks after implantation, respectively. At 5 weeks after implantation, spike signals from two mice were lost, and the Neurotassels recorded 25 neurons from five mice. At 6 weeks after implantation, the Neurotassels recorded 19 neurons from five mice, 9 of which have been stably recorded during the entire period. Figure 5D shows the spontaneous neuronal activity recorded by a microelectrode from 3 to 6 weeks after implantation. Principal components analysis (PCA) of the spike waveforms showed overlapping clusters across time (Fig. 5E). In addition, the interspike interval (ISI) histograms exhibited similar distribution patterns (Fig. 5F). These results suggested that the recorded spiking activities were from the same neuron. Notably, the good signal-to-noise ratio (SNR) of the spike waveforms suggested that the microelectrode-tissue interface was not degraded during the entire period. We further compared the chronic tissue response to our Neurotassels and to silicon probes using immunohistochemical analysis of brain slices (Fig. 5, G to L, and figs. S12 to S14). As shown in Fig. 5K, a silicon probe elicited clear neuronal cell loss around the probe surface after 5-week implantation, whereas minimal neuronal cell loss was observed around the Neurotassel implanted in the contralateral hemisphere of the same brain slice (Fig. 5H) (*12*, *15*, *24*, *27*, *30*). The close proximity of neurons to chronically implanted Neurotassels thus allowed stable neuronal activity recordings over extended periods (*6*, *48*). These results highlight the ability of

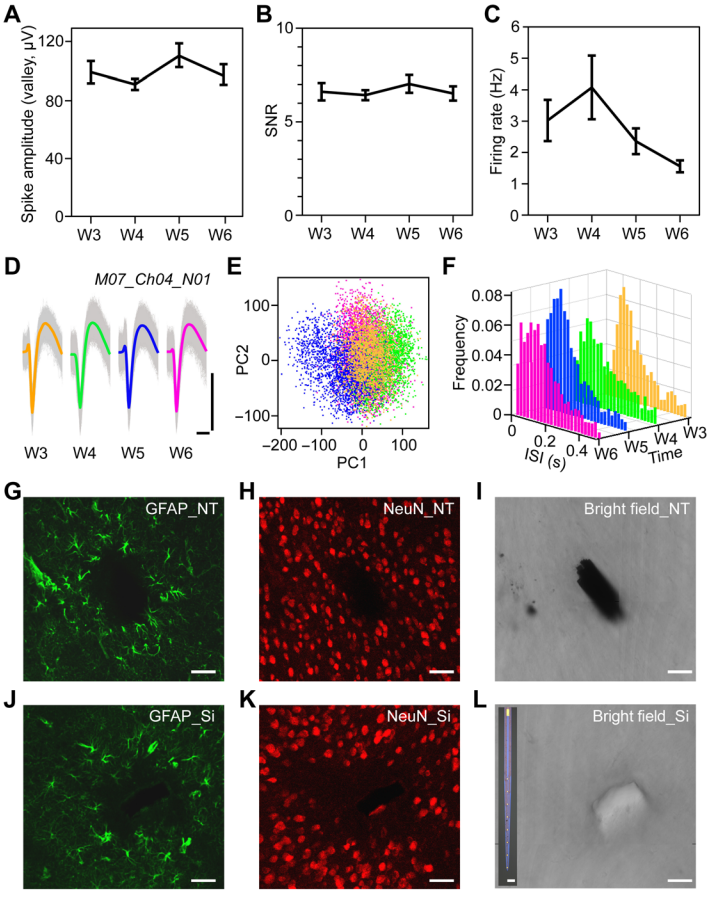

Fig. 5. Chronic stability of implanted Neurotassels. (**A** to **C**) Average spike amplitude, SNR, and firing rate of all sortable neurons recorded by Neurotassels from 3 to 6 weeks after implantation. Error bars represent SD around the mean. (**D**) Aligned and average spike waveforms recorded by a microelectrode of a 16-channel Neurotassel from 3 to 6 weeks after implantation. Scale bars, 100 μV (vertical), 1 ms (horizontal). (**E**) PCA of all waveforms in (D). (**F**) Time evolution of ISI histograms. Bin size, 20 ms. (**G** to **L**) Immunohistochemical staining and bright-field images of a horizontal brain slice after 5-week implantation of a Neurotassel and a silicon probe, respectively. The 100-μm-thick slice was labeled for astrocytes [glial fibrillary acidic protein (GFAP), green] and neurons (NeuN, red). Inset: A silicon probe with a cross-section of 100 × 30 μm^2. Scale bars, 50 μm (G to L), 100 μm (L, inset).

the flexible Neurotassels to form chronically stable interfaces with the nervous systems.

High scalability of Neurotassels

The development of implantable microelectrodes with high-density and large-number recording channels is critical for studying neural functions that involve large populations of neurons (*4*, *6*, *9*, *49*). Next, we demonstrate that the channel number of the Neurotassels could be readily scaled up to 128, 256, 512, and 1024 (fig. S15, A and B) while maintaining the small implantation footprints and low invasiveness. Figure 6 (A and B) and fig. S15C show Neurotassels with 128 and 256 microelectrode filaments, in which the 10-μm-diameter recording sites are arranged in a V shape. Each microelectrode filament has a cross-section of 10 × 1.5 μm^2. Neurotassels with 512 and 1024 microelectrode filaments are shown in Fig. 6 (C and D) and fig. S15D. The recording sites have a semicircular arch shape. Notably each microelectrode filament has an ultrasmall cross-section of 3 × 1.5 μm^2 (Fig. 6E), approaching the size of a neurite. As a result, the longitudinal bending stiffness of an individual microelectrode filament reached as low as 10^{-15} $N{\cdot}m^2$, which is more than six orders of magnitude lower than that of state-of-the-art silicon probes. After elastocapillary assembly, the obtained 128- and 1024-channel Neurotassel/PEG fibers have diameters of ca. 80 and 100 μm (Fig. 6, F and G), respectively. X-ray micro– and nano–computed tomography (micro- and nano-CT) imaging further revealed longitudinally distributed recording sites along the assembled fibers (fig. S15, E and F). Figure 6 (H and I) shows the cross-sections of the fibers, respectively. We systematically characterized the electrical performance of Neurotassels with different channel numbers. As shown in Fig. 6J, the Neurotassels have a device yield of >80% and an average impedance of 54 ± 15 kilohm after Pt electrodeposition, showing the good reliability of the manufacturing process. In addition, preliminary results verified the applicability of the 1024-channel Neurotassels for neural recordings (fig. S16).

DISCUSSION

Neurotassels that consist of arrays of flexible and high–aspect ratio microelectrode filaments have been fabricated by standard microfabrication techniques and assembled into implantable thin fibers by elastocapillary interactions. The Neurotassels can be readily scaled up to 1024 neurite-scale microelectrode filaments. The assembled microelectrode filaments were efficiently packed in three dimensions, similar to conventional microwire bundles, but with two orders of magnitude smaller cross-sections, longitudinally distributed recording sites, and easy electrical interconnections. Notably, nanofabrication techniques could allow further increase in channel number in each filament without increasing their implantation footprint. The ultrasmall sizes, high

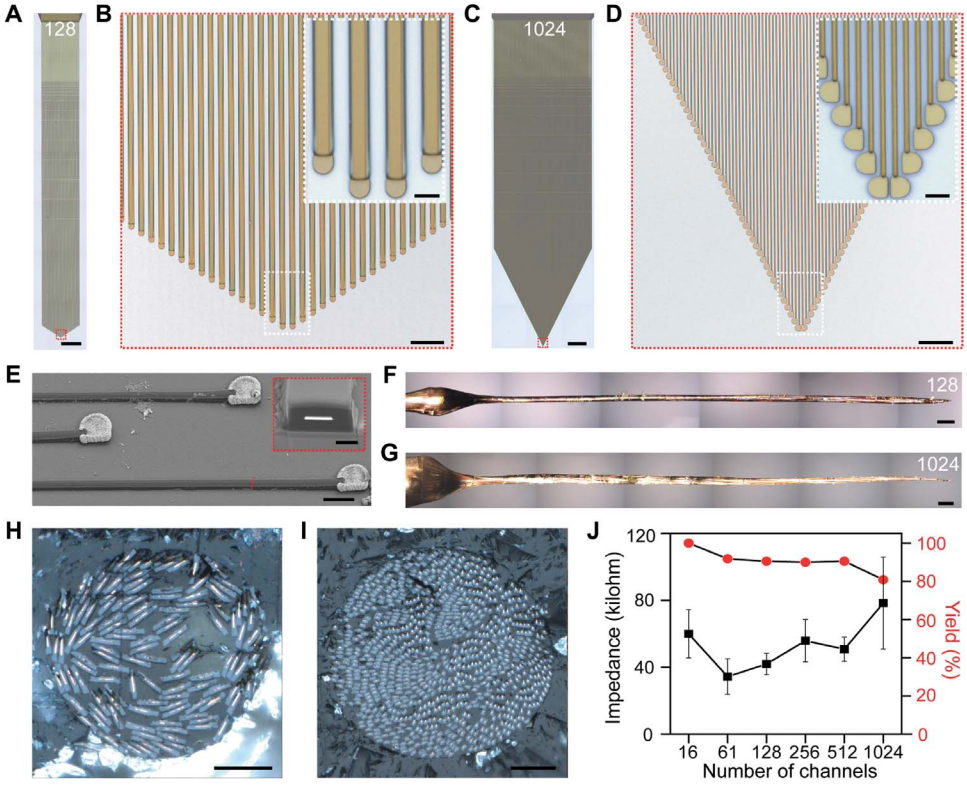

Fig. 6. Scalability of Neurotassels. (**A**) An as-fabricated 128-channel Neurotassel. Scale bar, 1 mm. (**B**) Zoom-in view of the microelectrode filaments in the red dashed box in (A). Scale bar, 50 μm. Inset: Zoom-in view in the white dashed box. Scale bar, 10 μm (inset). (**C**) An as-fabricated 1024-channel Neurotassel. Scale bar, 1 mm. (**D**) Zoom-in view of the microelectrode filaments in the red dashed box in (C). Scale bar, 50 μm. Inset: Zoom-in view in the white dashed box. Scale bar, 10 μm (inset). (**E**) An SEM image (tilted at 45°) of Pt-coated microelectrode filaments of a released 1024-channel Neurotassel. Scale bar, 10 μm. Inset: Focused ion beam–polished cross-section along the red dashed line. Scale bar, 1 μm (inset). (**F** and **G**) Assembled 128- and 1024-channel Neurotassel/PEG composite fibers, respectively. Scale bars, 200 μm. (**H** and **I**) Cross-sectional images of the assembled 128- and 1024-channel Neurotassel/PEG composite fibers, respectively. Scale bars, 20 μm. (**J**) Averaged impedance and yield of 16-, 61-, 128-, 256-, 512-, and 1024-channel Neurotassels after Pt electrodeposition. Error bars represent SE (n = 20).

flexibility, and scalability of Neurotassels make them suitable for chronic studies of large populations of neurons. Future studies are needed to integrate Neurotassels with on-chip amplifying and multiplexing circuitry to reduce the number of the external leads (*5*, *9*) and to develop biomimetic interfaces between the neurite-scale microelectrode filaments of Neurotassels and neural systems.

MATERIALS AND METHODS

Fabrication of Neurotassels

The Neurotassels were fabricated using standard microfabrication processes (fig. S1). The key fabrication steps are as follows: (i) A 10 cm silicon wafer (300-nm thermal oxide, Silicon Valley Microelectronics Inc.) was patterned with a 100-nm-thick aluminum release layer using photolithography (PL) (MA6 Mask Aligner, SUSS MicroTec Group) and e-beam evaporation (Ohmiker-50B, Cello Technology Co. Ltd.). (ii) A thin PI (U-Varnish S, UBE Industries, Ltd.) layer with a thickness of 0.75 or 2 μm was spin-coated and cured at 200°C for 2 hours in vacuum to form the bottom insulating layer. (iii) The wafer was spin-coated with LOR 3A lift-off resist (MicroChem) and baked at 170°C for 10 min, followed by spinning coating of Shipley S1813 positive photoresist (MICROPOSIT) and baking at 115°C for 3 min. The photoresist was patterned by PL. After developing in MF CD-26 (MICROPOSIT), the wafer was treated with reactive ion etching (RIE) [20 standard cubic centimeter per minute (SCCM) O_2, 200 W, 20 Pa, 5 s] (Etchlab 200, SENTECH Instruments GmbH). A 5-nm-thick chromium layer and a 100-nm-thick gold layer were sequentially deposited by e-beam evaporation to make the microelectrodes, interconnects, and bonding pads. (iv) A PI layer with a thickness of 0.75 μm was spin-coated onto the wafer and cured at 200°C for 2 hours to form the top insulating layer. (v) The wafer was patterned with AZ 4620 positive photoresist (Hoechst Celanese Corp.), and the PI was subsequently etched by RIE (20 sccm O_2, 200 W, 20 Pa, 3 to 6 min) to form the plane-mesh-filament segment and expose the recording sites at the front end and bonding pads at the rear end. For the 1024-channel Neurotassels, 100-nm-thick aluminum pattern was also used as etching mask during the RIE process. After lift-off, the wafer was rinsed with acetone and blow-dried with N_2. The wafer was cut into individual Neurotassels. The bonding pads at the rear end of the 16-channel Neurotassels were flip chip bonded to custom 0.3-mm-thick FPCs (16 positions, 0.5-mm pitch) using an anisotropic conductive film (MF331, Hitachi Ltd.) (fig. S3A). The 61-channel Neurotassels were bonded to standard 0.2-mm-thick FPCs (61 positions, 0.3-mm pitch, Shenzhen D&X Electronic Technology Co. Ltd.) using an anisotropic conductive film (fig. S3B). (vi) The Neurotassels were treated with oxygen plasma (20 sccm O_2, 100 W, 1 min) and then transferred to an etchant solution comprising 0.5 M $FeCl_3$ to remove the Al layer underneath the freestanding sections. The Neurotassels were rinsed with deionized water, and the silicon substrates were trimmed to the size of the contact region.

Microelectrode impedance measurements and electroplating

Impedance measurements were performed in phosphate-buffered saline (PBS; pH 7.4; HyClone Laboratories) at 1 kHz using an electrochemical workstation (Reference 3000, Gamry Instruments). Electrochemical impedance spectroscopy measurements were obtained by applying a 10-mV voltage from 10 to 100,000 Hz. A platinum rod was used as the counter electrode, and an Ag/AgCl electrode (CHI111, CH Instruments Inc.) was used as the reference electrode. The 0.3-mm-thick FPCs of the 16-channel Neurotassels were soldered to a 32-channel Omnetics connector (A79022-001, Omnetics Connector Corporation). The 0.2-mm-thick FPCs of the 61-channel Neurotassels were connected to a custom printed circuit board (PCB) through a low insertion force clip (FH23-61S-0.3SHW, Hirose). The PCB has two 32-channel A79022-001 Omnetics connectors. The 128-, 256-, 512-, and 1024-channel Neurotassels were measured in a probe station (TTP4, Lake Shore Cryotronics Inc.). Platinum was electroplated from an aqueous solution of 12 mM chloroplatinic acid (Shanghai Macklin Biochemical Co. Ltd.). The Gamry Reference 3000 electrochemical workstation was used to supply a constant potential of −0.1 V for 20 s. The Neurotassels were rinsed with deionized water after electroplating.

Elastocapillary assembly of Neurotassels

The Neurotassels were sterilized with 70% ethanol and then transferred to deionized water. To induce elastocapillary assembly, the Neurotassels were transferred into a molten PEG 4000 (95904, Sigma-Aldrich Co. LLC) bath at 120°C. PEG 4000 was used because of its good biocompatibility in the brain, low melting temperatures (T_g ~ 55°C), moderate viscosity (η ~ 200 centipoises), and relatively large surface tension (γ ~ 40 mN/m) (*50*–*53*). In addition, solidified PEG is stiff, with a Young's modulus of about 2 GPa (*54*), to penetrate into the brain tissue (*55*, *56*). The Neurotassels were secured to a micromanipulator (RWD Life Science Co. Ltd.), which withdrew the Neurotassels from the molten PEG bath into ambient air at a speed of ~1.5 mm/s. The capillary force of the molten PEG caused the elastic deformation of the Neurotassels. Along with the rapid solidification of the PEG, the mesh section formed a series of puffs, and the filaments were pulled together to form a thin fiber. A two-dimensional model is presented in fig. S5 to illustrate the capillary-driven bending deformation of the filaments at the mesh-filament transition zone of the Neurotassel/PEG composite fibers.

To study the dissolution behavior of the PEG in the Neurotassel/PEG composite fibers, 0.6% agar gel (K01001, Beijing Ke'erhui Technology Co. Ltd.) was used as the brain phantom because of its transparence and similar mechanical properties to brain tissues (*57*). Rhodamine B (RhB) (Beijing Ruitaibio Technology Co. Ltd.) dye was used as an indicator to monitor the dissolution of the PEG in the agar phantom. Prior to elastocapillary assembly, 1 ml of saturated RhB solution was added into 9-ml molten PEG 4000 at 60°C, followed by mixing for 5 min. A 16-channel Neurotassel was then transferred to the PEG/RhB bath and slowly withdrawn to form a Neurotassel/PEG/RhB composite fiber. The composite fiber was manually implanted ca. 5 mm into the agar phantom. The dissolution of the PEG and the release of the Neurotassel filaments were imaged under a microscope (fig. S6).

Implantation of Neurotassel/PEG fibers and neural activity recordings

All acute and chronic recordings were performed at the Institute of Neuroscience (ION) of the Chinese Academy of Sciences (CAS). Male adult C57BL/6 mice or Thy1-ChR2 mice were used for the current study. Wild-type mice (8 weeks, weighted between 20 and 30 g) were provided by the Shanghai Laboratory Animal Center, CAS (Shanghai, China). Thy1-ChR2 mice [B6.Cg-Tg(Thy1-COP4/EYFP)9Gfng/J, 8 weeks, weighted between 20 and 30 g] were provided by the Jackson Laboratory (ME, USA). Mice were group housed (four to six per cage) under a 12-hour light/12-hour dark cycle (lights on from 6:30 a.m. to 6:30 p.m.) at the Animal Resources Center of the ION. All animal

procedures complied with the National Institutes of Health *Guide for the Care and Use of Laboratory Animals* and were approved by the Animal Care and Use Committee of the ION. No statistical methods were used to predetermine sample size. The experiments were not randomized. Because of the technical nature of the study, the investigators were not blinded to allocation during experiments and outcome assessment.

Male adult C57BL/6 mice were used for neural activity recordings during a DPA task (Figs. 2 and 3). Before DPA training, Neurotassel/PEG fibers were implanted into the mPFC of six mice. Briefly, a mouse was anesthetized with intraperitoneally administrated pentobarbital sodium (0.01 g/ml; MYM Technologies Ltd.). The animal was placed in a standard rodent stereotaxic frame and positioned using ear bars. A stainless steel plate was fixed on the skull. A bare stainless steel wire was screw-secured into the contralateral hemisphere of the brain as the external ground. A square craniotomy of ca. 2 mm^2 was performed above the mPFC, and the dura was carefully removed. A Neurotassel/PEG assembly was fixed in a custom three-dimensional (3D) printed holder that was mounted on a micromanipulator. The Neurotassel/PEG fiber was then stereotaxically implanted into the mPFC of the mouse brain at a speed of ca. 2 mm/s and a depth of 2 mm. The probe above the brain surface was washed with artificial cerebrospinal fluid to dissolve the PEG. The holder was further moved downward for ca. 1 mm to accommodate the relative motion between the skull and the brain. The craniotomy was then covered with silicon elastomer Kwik-Sil (World Precision Instruments). The holder was fixed to the skull with dental acrylic (Shanghai New Century Dental Materials). The mice were given postsurgical intraperitoneal injection of antibiotic drug every day for 3 days. One week after surgery, the mice were trained to perform an olfactory DPA task for 13 days, and neural activities were recorded by the Neurotassels every day during the training. The 16-channel Neurotassels were connected to a 128-channel OmniPlex amplifier (Plexon Inc.). Electrophysiological recording was performed at a sampling rate of 40 kHz. A 250-Hz high-pass filter was applied for single-unit recordings. Spike detection and sorting were performed using OmniPlex and Offline Sorter (Plexon Inc.) by projecting waveforms into principal component space and identifying isolated clusters.

In Fig. 3A, the activities for the same neuron across different training days were averaged as one row. The color bar indicates the *Z*-score normalization calculated from the cross-trial mean and SD during the baseline period. The normalized firing rate is defined as the raw firing rate subtracting the mean of baseline firing across all trials and dividing the SD of baseline firing across trials

$$\text{Normalized firing rate} = \frac{\text{Average raw firing rate} - \text{average baseline firing rate}}{\text{SD of baseline firing rate across trials}}$$

Baseline firing rate is defined as the firing rate during −3 to −1 s before sample odor delivery. Note that this normalized firing rate represents the firing modulation of neurons during task events.

For long-term chronic recordings in Fig. 5 (A to F), 16-channel Neurotassel/PEG fibers were implanted into the mPFC of seven male adult C57BL/6 mice (8 weeks, 25 g). Electrophysiological recordings were performed on the awake mice every week from week 3. A microelectrode was chosen as the internal reference in case of loss of the external reference. Electrophysiological recordings were performed at a sampling rate of 40 kHz. A 250-Hz high-pass filter was applied for single-unit recordings. Spike detection and sorting were performed using OmniPlex and Offline Sorter. Each average waveform in Fig. 5D was calculated from 2000 waveforms.

For acute optogenetics experiments in Fig. 4 and fig. S10, Thy1-ChR2 mice (8 weeks, ca. 25 g) were used. A homemade 3D printed holder was designed to house a 61-channel Neurotassel assembled on a sharpened optical fiber (Plexon Inc.) (Fig. 4A). The front end of the Neurotassel was located ~150 μm below the tip of the optical fiber (Fig. 4B). The Neurotassel/optical fiber probe was implanted into the mPFC (position according to bregma: anteroposterior, +1.98 mm; mediolateral, 0.40 mm; dorsoventral, 1.60 mm). The Neurotassel was connected to a 128-channel OmniPlex amplifier for electrophysiological recordings. Light (473 nm) was generated by a diode laser (Shanghai Laser & Optics Century Co. Ltd.) and delivered through the optical fiber. Light was delivered in a square wave pattern of variable frequency, duration, and on-off cycle. The peak light power was approximately 2 mW. The average waveforms in Fig. 4D were calculated from 1200 (black, no light emission) and 100 (blue, 473-nm emission) waveforms, respectively.

Optical stimulation artifacts were removed from the recording data by using a common average referencing (CAR) method (*9*, *58*, *59*). Electrical signals were recorded by a microelectrode during optogenetic stimulation (5-ms pulse, 10 or 20 Hz). The signals were high pass filtered with a cutoff frequency of 250 Hz. Figure S10C (top) shows representative electrical signals recorded from 20 repeated trials. As shown in the magnified image in fig. S10C (middle), the signals from different trials showed nearly identical optical stimulation artifacts. We then applied a CAR filter by computing the median signal across all trials and then subtracting this value from each trial. As shown in fig. S10C (bottom), the CAR filter effectively removed the artifacts related to light stimulation.

Behavior training

Some of the following methods are similar to those previously published (*43*). Before behavioral training, mice were housed under stable conditions with food and water ad libitum. After the start of behavioral training, water supply was restricted. Mice could drink water only during and immediately after training. Care was taken to keep mice body weight above 80% of normal level.

In a DPA task, a sample olfactory stimulus (S1 or S2; S1: butyl formate, S2: 1-pentanol) was presented at the start of a trial, followed by a delay period (5 s) and then a testing stimulus (T1 or T2; T1: ethyl acetate, T2: methyl butenol). Odor delivery duration was set to 1 s, which was sufficient for rodents to perceive olfactory cues. Mice were trained to lick in the response window. The response window (0.5 s in duration) was started 1 s after the offset of the second odor delivery. Licking events detected in the response window in paired trials (S1-T1 or S2-T2) were regarded as Hit and will trigger instantaneous water delivery (50 ms in duration). False choice was defined as detection of licking events in the response window in unpaired (DPA) trials, and mice were not punished in "false alarm" trials. Mice were neither punished nor rewarded for "miss" (no-lick in a paired trial) nor "correct rejection" (no-lick in unpaired trial) trials. Licking events were detected by infrared beam breakers. Odor and water delivery, laser illumination, and licking events were recorded by computers through serial ports. In each day, mice were required to perform 100 trials for the DPA task in optogenetic and electrophysiological experiments. After the training sessions ended each day, mice were supplied with free water until satiety.

Before the start of training, mice were water restricted for 2 days. The behavioral training process included habituation, shaping, and

task-learning phases. In the habituation phase, mice were head fixed in behavioral setups and trained to lick water from a water tube, encouraged with automatically delivered water through rodent lavage needles. Typically, mice could learn to lick for 1 to 2 min continuously in 1 to 2 days. The shaping phase was then started, in which only paired trials were applied and water was provided in all trials each day. In the beginning of the shaping phase, water was delivered manually through syringes to encourage mice to lick in the response window for only 10 trials. For the rest trials, mice were trained automatically. The shaping phase typically lasted for 2 to 3 days. The task-learning phase was then started from the next day, which was defined as day 1 in the behavioral analysis reported in all figures. All kinds of trials were applied pseudorandomly, i.e., two paired and two unpaired trials of balanced odor pairs were presented randomly in every four consecutive trials in the DPA task. No human intervention was applied in the task-learning phase to minimize any potential human bias in the behavioral results.

The performance correct rate (referred to as "performance" in labels of Fig. 2B) of each batch of 20 trials was defined by

$$\text{Performance (correct rate)} = \frac{\text{Number of hit trials} + \text{Number of correct rejection trials}}{\text{Total number of trials}}$$

Histological sample preparation

The immunohistological experiments were performed at the National Center for Nanoscience and Technology (NCNST), China. All animal procedures complied with the National Institutes of Health *Guide for the Care and Use of Laboratory Animals* and were approved by the Animal Care and Use Committee of the NCNST.

Neurotassels were implanted into the mPFC of mice, and silicon probes with a width of 100 μm (gradually tapering to the tip) and a thickness of 30 μm were implanted into the contralateral hemispheres. Five weeks after implantation, the mice were administrated with intraperitoneal injection of sodium pentobarbital and then transcardially perfused with 1× PBS and 4% paraformaldehyde. The mice were decapitated, and the brain was carefully removed. The brain was cryoprotected in 4% paraformaldehyde solution overnight and then sectioned into 100-μm-thick slices perpendicular to the probes using a vibrating blade microtome (VT1200S, Leica Biosystems). Brain slices were incubated in 0.3% Triton X-100 at 25°C for 15 min to increase the permeability of the membrane. Then, the slices were incubated in blocking solution consisting of 3% bovine serum albumin for 1 hour at 25°C. After that, the slices were incubated in primary antibodies (1:200 dilution, MAB377 for neurons, Millipore; 1:1000 dilution, Z033429 for astrocytes, Agilent Technologies) overnight at 4°C. After antibody incubation, the slices were rinsed three times with PBS. Then, the slices were incubated in fluorophore-conjugated antibodies for 2 hours. Antibodies used for different cell types are as follows: goat anti-mouse immunoglobulin G (IgG) [heavy and light chains (H + L)] secondary antibody 633 (1:1000 dilution, A21050, Invitrogen) for neurons and goat anti-rabbit IgG (H + L) secondary antibody 488 (1:1000 dilution, A11008, Invitrogen) for astrocytes. Last, the slices were rinsed three times with PBS and put on the glass slide. Confocal fluorescence imaging of the slices was acquired on a Zeiss LSM 710 confocal microscope (Carl Zeiss) using 488- and 633-nm lasers as the excitation sources for Alexa Fluor 488 and Alexa Fluor 633, respectively.

Microglial activation was characterized by immunohistochemistry staining using Iba1 as marker. Briefly, 0.01 M citrate antigen retrieval solution (pH 6.0) was heated to boil, and then, the slices were boiled for 10 min for antigen retrieval. After natural cooling, the slices were incubated in 0.3% Triton X-100 at 25°C for 15 min to increase the permeability of the membrane. Then, the slices were incubated in blocking solution consisting of 3% bovine serum albumin for 1 hour at 25°C. After that, the slices were incubated in Iba1 primary antibody (1:100 dilution, ab153696, Abcam) overnight and goat anti-rabbit IgG (H + L) secondary antibody 488 (1:1000 dilution, A11008, Invitrogen) for 2 hours. Last, confocal microscopy images were recorded using a 488-nm laser.

Structural and fluorescence imaging

Optical images of samples were acquired on an Olympus LEXT OLS4000 laser scanning confocal microscope, a Leica DM4 M microscope (Leica Biosystems), and an Olympus BX51 microscope (Olympus Corporation). Full images of the devices and Neurotassel/PEG fibers in Figs. 1 (A and F) and 6 (A, C, F, and G) and figs. S2A and S15G were obtained by the automated acquisition and stitching software of the microscopes. For cross-sectional imaging (Figs. 1, I and J, and 6, H and I), the Neurotassel/PEG assemblies were embedded in PEG matrices and cross sectioned using a Leica VT1200S semi-automatic vibrating blade microtome. Scanning electron microscopy (SEM) images (Figs. 1B and 6E) were collected using a Nova Nanolab 200 FIB/SEM dual-beam system (FEI) at 5 kV. The cross-section of the filament in Fig. 6E was prepared by focused ion beam (FIB) milling. Before milling, a thin platinum layer was deposited by FIB on the sample surface using a $CH_3C_5H_4Pt(CH_3)_3$ gas source. Micro- and nano-CT images of 128- and 1024-channel Neurotassel/PEG composite fibers in fig. S15 (E and F) were acquired using Zeiss Xradia 520 Versa and 800 Ultra 3D X-ray microscopes (Carl Zeiss X-ray Microscopy Inc.), respectively. The tube voltage of the Zeiss Xradia 520 Versa was set to 80 kV. The Zeiss Xradia 800 Ultra used an 8-keV laboratory X-ray source. After scanning, the acquired radiography images were reconstructed into a 3D volume using the ZEISS XMReconstructor software.

SUPPLEMENTARY MATERIALS

Supplementary material for this article is available at http://advances.sciencemag.org/cgi/content/full/5/3/eaav2842/DC1

Fig. S1. Schematics of Neurotassel fabrication steps.
Fig. S2. 61-channel Neurotassels.
Fig. S3. Flip chip–bonded 16- and 61-channel Neurotassels.
Fig. S4. Simulated deformation and von Mises stresses in Neurotassels.
Fig. S5. Elastocapillary assembly of Neurotassels with water and PEG.
Fig. S6. Implantation of Neurotassel/PEG composite fiber in brain phantom.
Fig. S7. Simultaneous recordings from aPC and pPC by two Neurotassels.
Fig. S8. Time-dependent analysis of all recorded spiking activities during behavior training.
Fig. S9. Time-dependent analysis of the spiking activities of two example neurons during behavioral training.
Fig. S10. Simultaneous optical stimulation and electrical recordings with Neurotassel/optical fiber dual-functional probes.
Fig. S11. Long-term recording stability of Neurotassels.
Fig. S12. Chronic tissue response of Neurotassel and silicon probe after 5-week implantation.
Fig. S13. Chronic tissue response of implanted probes.
Fig. S14. Microglial activation in response to chronically implanted Neurotassel and silicon probe.
Fig. S15. High-density Neurotassels.
Fig. S16. Recordings with 1024-channel Neurotassels.
Movie S1. Released Neurotassel.
Movie S2. Elastocapillary assembly of Neurotassel.

Movie S3. Depth implantation of Neurotassel in brain.
Movie S4. Dissolution of PEG of Neurotassel/PEG fiber in the brain.
Movie S5. Simultaneous optogenetic stimulation and recording with assembled Neurotassel/optical fiber probe.
Movie S6. Mice with chronically implanted Neurotassels.
Reference (*60*)

REFERENCES AND NOTES

1. P. K. Campbell, K. E. Jones, R. J. Huber, K. W. Horch, R. A. Normann, A silicon-based, three-dimensional neural interface: Manufacturing processes for an intracortical electrode array. *IEEE Trans. Biomed. Eng.* **38**, 758–768 (1991).
2. C. M. Gray, P. E. Maldonado, M. Wilson, B. McNaughton, Tetrodes markedly improve the reliability and yield of multiple single-unit isolation from multi-unit recordings in cat striate cortex. *J. Neurosci. Methods* **63**, 43–54 (1995).
3. M. A. L. Nicolelis, D. Dimitrov, J. M. Carmena, R. Crist, G. Lehew, J. D. Kralik, S. P. Wise, Chronic, multisite, multielectrode recordings in macaque monkeys. *Proc. Natl. Acad. Sci. U.S.A.* **100**, 11041–11046 (2003).
4. J. Csicsvari, D. A. Henze, B. Jamieson, K. D. Harris, A. Sirota, P. Barthó, K. D. Wise, G. Buzsáki, Massively parallel recording of unit and local field potentials with silicon-based electrodes. *J. Neurophysiol.* **90**, 1314–1323 (2003).
5. K. D. Wise, D. J. Anderson, J. F. Hetke, D. R. Kipke, K. Najafi, Wireless implantable microsystems: High-density electronic interfaces to the nervous system. *Proc. IEEE* **92**, 76–97 (2004).
6. G. Buzsáki, Large-scale recording of neuronal ensembles. *Nat. Neurosci.* **7**, 446–451 (2004).
7. D. B. T. McMahon, I. V. Bondar, O. A. T. Afuwape, D. C. Ide, D. A. Leopold, One month in the life of a neuron: Longitudinal single-unit electrophysiology in the monkey visual system. *J. Neurophysiol.* **112**, 1748–1762 (2014).
8. T. Aflalo, S. Kellis, C. Klaes, B. Lee, Y. Shi, K. Pejsa, K. Shanfield, S. Hayes-Jackson, M. Aisen, C. Heck, C. Liu, R. A. Andersen, Decoding motor imagery from the posterior parietal cortex of a tetraplegic human. *Science* **348**, 906–910 (2015).
9. J. J. Jun, N. A. Steinmetz, J. H. Siegle, D. J. Denman, M. Bauza, B. Barbarits, A. K. Lee, C. A. Anastassiou, A. Andrei, Ç. Aydın, M. Barbic, T. J. Blanche, V. Bonin, J. Couto, B. Dutta, S. L. Gratiy, D. A. Gutnisky, M. Häusser, B. Karsh, P. Ledochowitsch, C. M. Lopez, C. Mitelut, S. Musa, M. Okun, M. Pachitariu, J. Putzeys, P. D. Rich, C. Rossant, W.-l. Sun, K. Svoboda, M. Carandini, K. D. Harris, C. Koch, J. O'Keefe, T. D. Harris, Fully integrated silicon probes for high-density recording of neural activity. *Nature* **551**, 232–236 (2017).
10. P. J. Rousche, R. A. Normann, Chronic recording capability of the Utah intracortical electrode array in cat sensory cortex. *J. Neurosci. Methods* **82**, 1–15 (1998).
11. J. C. Williams, R. L. Rennaker, D. R. Kipke, Long-term neural recording characteristics of wire microelectrode arrays implanted in cerebral cortex. *Brain Res. Brain Res. Protoc.* **4**, 303–313 (1999).
12. R. Biran, D. C. Martin, P. A. Tresco, Neuronal cell loss accompanies the brain tissue response to chronically implanted silicon microelectrode arrays. *Exp. Neurol.* **195**, 115–126 (2005).
13. V. S. Polikov, P. A. Tresco, W. M. Reichert, Response of brain tissue to chronically implanted neural electrodes. *J. Neurosci. Methods* **148**, 1–18 (2005).
14. A. Gilletti, J. Muthuswamy, Brain micromotion around implants in the rodent somatosensory cortex. *J. Neural Eng.* **3**, 189–195 (2006).
15. G. C. McConnell, H. D. Rees, A. I. Levey, C.-A. Gutekunst, R. E. Gross, R. V. Bellamkonda, Implanted neural electrodes cause chronic, local inflammation that is correlated with local neurodegeneration. *J. Neural Eng.* **6**, 056003 (2009).
16. P. J. Rousche, D. S. Pellinen, D. P. Pivin Jr., J. C. Williams, R. J. Vetter, D. R. Kipke, Flexible polyimide-based intracortical electrode arrays with bioactive capability. *IEEE Trans. Biomed. Eng.* **48**, 361–371 (2001).
17. T. D. Y. Kozai, N. B. Langhals, P. R. Patel, X. Deng, H. Zhang, K. L. Smith, J. Lahann, N. A. Kotov, D. R. Kipke, Ultrasmall implantable composite microelectrodes with bioactive surfaces for chronic neural interfaces. *Nat. Mater.* **11**, 1065–1073 (2012).
18. B. Tian, J. Liu, T. Dvir, L. Jin, J. H. Tsui, Q. Qing, Z. Suo, R. Langer, D. S. Kohane, C. M. Lieber, Macroporous nanowire nanoelectronic scaffolds for synthetic tissues. *Nat. Mater.* **11**, 986–994 (2012).
19. G. Guitchounts, J. E. Markowitz, W. A. Liberti, T. J. Gardner, A carbon-fiber electrode array for long-term neural recording. *J. Neural Eng.* **10**, 046016 (2013).
20. T.-i. Kim, J. G. McCall, Y. H. Jung, X. Huang, E. R. Siuda, Y. Li, J. Song, Y. M. Song, H. A. Pao, R.-H. Kim, C. Lu, S. D. Lee, I.-S. Song, G. Shin, R. Al-Hasani, S. Kim, M. P. Tan, Y. Huang, F. G. Omenetto, J. A. Rogers, M. R. Bruchas, Injectable, cellular-scale optoelectronics with applications for wireless optogenetics. *Science* **340**, 211–216 (2013).
21. J. K. Nguyen, D. J. Park, J. L. Skousen, A. E. Hess-Dunning, D. J. Tyler, S. J. Rowan, C. Weder, J. R. Capadona, Mechanically-compliant intracortical implants reduce the neuroinflammatory response. *J. Neural Eng.* **11**, 056014 (2014).
22. D. Khodagholy, J. N. Gelinas, T. Thesen, W. Doyle, O. Devinsky, G. G. Malliaras, G. Buzsáki, NeuroGrid: Recording action potentials from the surface of the brain. *Nat. Neurosci.* **18**, 310–315 (2015).
23. D.-H. Kim, J. Viventi, J. J. Amsden, J. Xiao, L. Vigeland, Y.-S. Kim, J. A. Blanco, B. Panilaitis, E. S. Frenchette, D. Contreras, D. L. Kaplan, F. G. Omenetto, Y. Huang, K.-C. Hwang, M. R. Zakin, B. Litt, J. A. Rogers, Dissolvable films of silk fibroin for ultrathin conformal bio-integrated electronics. *Nat. Mater.* **9**, 511–517 (2010).
24. J. Liu, T.-M. Fu, Z. Cheng, G. Hong, T. Zhou, L. Jin, M. Duvvuri, Z. Jiang, P. Kruskal, C. Xie, Z. Suo, Y. Fang, C. M. Lieber, Syringe-injectable electronics. *Nat. Nanotechnol.* **10**, 629–636 (2015).
25. C. Xie, J. Liu, T.-M. Fu, X. Dai, W. Zhou, C. M. Lieber, Three-dimensional macroporous nanoelectronic networks as minimally invasive brain probes. *Nat. Mater.* **14**, 1286–1292 (2015).
26. A. Canales, X. Jia, U. P. Froriep, R. A. Koppes, C. M. Tringides, J. Selvidge, C. Lu, C. Hou, L. Wei, Y. Fink, P. Anikeeva, Multifunctional fibers for simultaneous optical, electrical and chemical interrogation of neural circuits in vivo. *Nat. Biotechnol.* **33**, 277–284 (2015).
27. L. Luan, X. Wei, Z. Zhao, J. J. Siegel, O. Potnis, C. A. Tuppen, S. Lin, S. Kazmi, R. A. Fowler, S. Holloway, A. K. Dunn, R. A. Chitwood, C. Xie, Ultraflexible nanoelectronic probes form reliable, glial scar-free neural integration. *Sci. Adv.* **3**, e1601966 (2017).
28. T. D. Y. Kozai, D. R. Kipke, Insertion shuttle with carboxyl terminated self-assembled monolayer coatings for implanting flexible polymer neural probes in the brain. *J. Neurosci. Methods* **184**, 199–205 (2009).
29. G. Lind, C. E. Linsmeier, J. Thelin, J. Schouenborg, Gelatine-embedded electrodes—A novel biocompatible vehicle allowing implantation of highly flexible microelectrodes. *J. Neural Eng.* **7**, 046005 (2010).
30. T. D. Y. Kozai, Z. Gugel, X. Li, P. J. Gilgunn, R. Khilwani, O. B. Ozdoganlar, G. K. Fedder, D. J. Weber, X. T. Cui, Chronic tissue response to carboxymethyl cellulose based dissolvable insertion needle for ultra-small neural probes. *Biomaterials* **35**, 9255–9268 (2014).
31. Z. Xiang, S.-C. Yen, N. Xue, T. Sun, W. M. Tsang, S. Zhang, L.-D. Liao, N. V. Thakor, C. Lee, Ultra-thin flexible polyimide neural probe embedded in a dissolvable maltose-coated microneedle. *J. Micromech. Microeng.* **24**, 065015 (2014).
32. S. Takeuchi, D. Ziegler, Y. Yoshida, K. Mabuchi, T. Suzuki, Parylene flexible neural probes integrated with microfluidic channels. *Lab Chip* **5**, 519–523 (2005).
33. F. Vitale, D. G. Vercosa, A. V. Rodriguez, S. S. Pamulapati, F. Seibt, E. Lewis, J. S. Yan, K. Badhiwala, M. Adnan, G. Royer-Carfagni, M. Beierlein, C. Kemere, M. Pasquali, J. T. Robinson, Fluidic microactuation of flexible electrodes for neural recording. *Nano Lett.* **18**, 326–335 (2018).
34. J. Agorelius, F. Tsanakalis, A. Friberg, P. T. Thorbergsson, L. M. E. Pettersson, J. Schouenborg, An array of highly flexible electrodes with a tailored configuration locked by gelatin during implantation—Initial evaluation in cortex cerebri of awake rats. *Front. Neurosci.* **9**, 331 (2015).
35. T.-M. Fu, G. Hong, R. D. Viveros, T. Zhou, C. M. Lieber, Highly scalable multichannel mesh electronics for stable chronic brain electrophysiology. *Proc. Natl. Acad. Sci. U.S.A.* **114**, E10046–E10055 (2017).
36. J. Bico, B. Roman, L. Moulin, A. Boudaoud, Elastocapillary coalescence in wet hair. *Nature* **432**, 690–690 (2004).
37. C. Duprat, S. Protière, A. Y. Beebe, H. A. Stone, Wetting of flexible fibre arrays. *Nature* **482**, 510–513 (2012).
38. B. Pokroy, S. H. Kang, L. Mahadevan, J. Aizenberg, Self-organization of a mesoscale bristle into ordered, hierarchical helical assemblies. *Science* **323**, 237–240 (2009).
39. N. Chakrapani, B. Wei, A. Carrillo, P. M. Ajayan, R. S. Kane, Capillarity-driven assembly of two-dimensional cellular carbon nanotube foams. *Proc. Natl. Acad. Sci. U.S.A.* **101**, 4009–4012 (2004).
40. H. Liu, S. Li, J. Zhai, H. Li, Q. Zheng, L. Jiang, D. Zhu, Self-assembly of large-scale micropatterns on aligned carbon nanotube films. *Angew. Chem. Int. Ed.* **43**, 1146–1149 (2004).
41. P. R. Patel, K. Na, H. Zhang, T. D. Y. Kozai, N. A. Kotov, E. Yoon, C. A. Chestek, Insertion of linear 8.4 μm diameter 16 channel carbon fiber electrode arrays for single unit recordings. *J. Neural Eng.* **12**, 046009 (2015).
42. A. Baddeley, Working memory: Theories, models, and controversies. *Annu. Rev. Psychol.* **63**, 1–29 (2012).
43. D. Liu, X. Gu, J. Zhu, X. Zhang, Z. Han, W. Yan, Q. Cheng, J. Hao, H. Fan, R. Hou, Z. Chen, Y. Chen, C. T. Li, Medial prefrontal activity during delay period contributes to learning of a working memory task. *Science* **346**, 458–463 (2014).
44. Z. Han, X. Zhang, J. Zhu, Y. Chen, C. T. Li, High-throughput automatic training system for odor-based learned behaviors in head-fixed mice. *Front. Neural Circuits* **12**, 15 (2018).
45. G. Buzsáki, *Rhythms of the Brain* (Oxford Univ. Press, 2006).
46. J. M. Bekkers, N. Suzuki, Neurons and circuits for odor processing in the piriform cortex. *Trends Neurosci.* **36**, 429–438 (2013).

47. E. S. Boyden, F. Zhang, E. Bamberg, G. Nagel, K. Deisseroth, Millisecond-timescale, genetically targeted optical control of neural activity. *Nat. Neurosci.* **8**, 1263–1268 (2005).
48. K. D. Harris, R. Q. Quiroga, J. Freeman, S. L. Smith, Improving data quality in neuronal population recordings. *Nat. Neurosci.* **19**, 1165–1174 (2016).
49. G. Rios, E. V. Lubenov, D. Chi, M. L. Roukes, A. G. Siapas, Nanofabricated neural probes for dense 3-D recordings of brain activity. *Nano Lett.* **16**, 6857–6862 (2016).
50. K. B. Bjugstad, K. Lampe, D. S. Kern, M. Mahoney, Biocompatibility of poly(ethylene glycol)-based hydrogels in the brain: An analysis of the glial response across space and time. *J. Biomed. Mater. Res. A* **95A**, 79–91 (2010).
51. G. R. Lloyd, D. Q. M. Craig, A. Smith, An investigation into the melting behavior of binary mixes and solid dispersions of paracetamol and PEG 4000. *J. Pharm. Sci.* **86**, 991–996 (1997).
52. M. Iguchi, Y. Hiraga, K. Kasuya, T. M. Aida, M. Watanabe, Y. Sato, R. L. Smith Jr., Viscosity and density of poly(ethylene glycol) and its solution with carbon dioxide at 353.2 K and 373.2 K at pressures up to 15 MPa. *J. Supercrit. Fluids* **97**, 63–73 (2015).
53. J. M. Harris, S. Zalipsky, *Poly (Ethylene Glycol): Chemistry and Biological Applications* (vol. 680 of ACS Symposium Series, American Chemical Society, 1997).
54. M. A. Al-Nasassrah, F. Podczeck, J. M. Newton, The effect of an increase in chain length on the mechanical properties of polyethylene glycols. *Eur. J. Pharm. Biopharm.* **46**, 31–38 (1998).
55. J. Subbaroyan, D. C. Martin, D. R. Kipke, A finite-element model of the mechanical effects of implantable microelectrodes in the cerebral cortex. *J. Neural Eng.* **2**, 103–113 (2005).
56. A. K. Ommaya, Mechanical properties of tissues of the nervous system. *J. Biomech.* **1**, 127–138 (1968).
57. N. H. Hosseini, R. Hoffmann, S. Kisban, T. Stieglitz, O. Paul, P. Ruther, Comparative study on the insertion behavior of cerebral microprobes. *Conf. Proc. IEEE Eng. Med. Biol. Soc.* **2007**, 4711–4714 (2007).
58. J. D. Rolston, R. E. Gross, S. M. Potter, Common median referencing for improved action potential detection with multielectrode arrays. *Conf. Proc. IEEE Eng. Med. Biol. Soc.* **2009**, 1604–1607 (2009).
59. K. A. Ludwig, R. M. Miriani, N. B. Langhals, M. D. Joseph, D. J. Anderson, D. R. Kipke, Using a common average reference to improve cortical neuron recordings from microelectrode arrays. *J. Neurophysiol.* **101**, 1679–1689 (2009).
60. B. Roman, J. Bico, Elasto-capillarity: Deforming an elastic structure with a liquid droplet. *J. Phys. Condens. Matter* **22**, 493101 (2010).

Acknowledgments: We thank the Fabrication Lab at NCNST for the microfabrication facilities and support, and the Animal Resource Center at ION for animal housing and care. We thank M.-m. Poo and C. M. Lieber for the comments on the manuscript and J. Pan, Z. Wang, T. Yang, and Y. Gu for the valuable discussions. **Funding:** This work was supported by the National Natural Science Foundation of China (21790393, 21673057, and 31525010), CAS Instrument Developing Project (YZ201540), CAS Key Research Program of Frontier Sciences (QYZDB-SSW-SMC009), and the Shanghai Municipal Science and Technology Major Project (grant no. 2018SHZDZX05). **Author contributions:** Y.F. conceived the idea. Y.F. and C.L. designed the experiments. S.G., J.W., L.Z., and M.D. fabricated and characterized the devices. X.G., R.H., and H.F. performed the surgery, electrophysiological recording, behavior training, and corresponding analysis. S.G., J.W., and L.G. performed the histology. Y.Z. and Y.F. performed the mechanical simulations. Y.F. and C.L. wrote the manuscript with input from all authors. **Competing interests:** Y.F., J.W., M.D., and S.G. are inventors on a patent application related to this work (application no. CN106667475A; filed on 20 December 2016 by the NCNST). Y.F., J.W., S.G., M.D., and L.Z. are inventors on an additional patent application related to this work (application no. WO2018113073A1; filed on 06 February 2017 by the NCNST). Both patents cover Neurotassels and their uses. All the other authors declare that they have no competing interests. **Data and materials availability:** All data needed to evaluate the conclusions in the paper are present in the paper and/or the Supplementary Materials. Additional data related to this paper may be requested from the authors.

Submitted 1 September 2018
Accepted 6 February 2019
Published 27 March 2019
10.1126/sciadv.aav2842

Citation: S. Guan, J. Wang, X. Gu, Y. Zhao, R. Hou, H. Fan, L. Zou, L. Gao, M. Du, C. Li, Y. Fang, Elastocapillary self-assembled neurotassels for stable neural activity recordings. *Sci. Adv.* **5**, eaav2842 (2019).